

pubs.acs.org/cm Article

# Role of Cr Redox and Dynamics in Electrochemical Cycling of $H_xCrS_{2-\delta}$

Joseph W. Stiles, Brianna Hoff, Maria C. Curria, Scott B. Lee, Fang Yuan, Guangming Cheng, Fatmagül Katmer, Grigorii Skorupskii, Jiaze Xie, Josh Leeman, Nan Yao, Claire E. White, Craig B. Arnold, and Leslie M. Schoop\*



Cite This: Chem. Mater. 2024, 36, 9469-9479



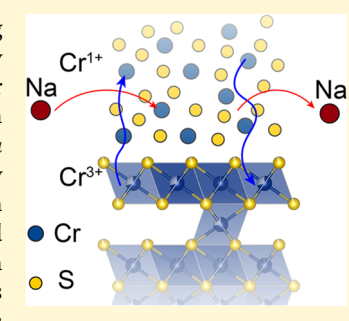
**ACCESS** 

Metrics & More



Supporting Information

**ABSTRACT:**  $H_x CrS_{2-\delta}$  is produced by the proton exchange of  $NaCrS_2$  and features alternating layers of crystalline and amorphous lamella. It exhibits superior performance as a Na-ion battery electrode compared with its parent compound with faster  $Na^+$  diffusion, higher capacity, and better cyclability. This work explores the nature of the unique biphasic structure of  $H_x CrS_{2-\delta}$  using both powder and single-crystal X-ray diffraction, as well as electron microscopy. Additionally, *ex situ* characterizations using X-ray absorption spectroscopy, X-ray total scattering, and magnetometry are employed to study the mechanism by which this superiority arises. These reveal that migration of Cr does not impede battery performance and may, in fact, be crucial to the observed performance improvements. These studies show that Cr redox is not only possible but abundant in  $H_x CrS_{2-\delta}$  while accessing it in  $NaCrS_2$  at lower voltages results in irreversible structural transitions that limit cycling stability. Additionally, we highlight the potential of biphasic structures such as  $H_x CrS_{2-\delta}$  to enable high performance in energy storage electrodes.



### ■ INTRODUCTION

A growing body of recent literature has highlighted the role of transition metal migration in energy storage systems and how its detrimental effects may be avoided. <sup>1–6</sup> It is, at this point, well-known that transition metal migration in layered materials and a hysteretic voltage profile are correlated and that, in extreme cases, migration may result in disproportionation and complete dissolution of the transition metal ion into the electrolyte. <sup>7,8</sup> The traditional method to prevent these problems is simply to limit the cell voltage, thereby preventing transition metal migration from occurring, as was done in LiCoO<sub>2</sub> to enable its commercialization. <sup>8,9</sup> However, this limits the electrode to only a fraction of its theoretical capacity, as complete deintercalation of the alkali ion is precluded by the voltage constraint.

Recently, several methods to alleviate these effects by preventing or augmenting transition metal migration have been investigated. For example, it has been noted that introducing disorder to the structure of the electrode inhibits or hinders this migration, resulting in longer-lasting electrodes with better performance. <sup>1,4</sup> In particular, several publications have utilized structural or compositional defects either in the transition metal coordination or the alkali cation site to introduce disorder with some success in preventing voltage hysteresis. <sup>1,5</sup> Some of these efforts have focused on disorder at the transition metal site through the mixing of the alkali metal onto the site, which eliminates "collective" migration while allowing random migration of the transition metal. Others have investigated the

effects of transition metal vacancies to allow reversible migration of the metal. 10

While most of the literature on mitigating the effects of transition metal migration focuses on lithium metal oxides, the problem persists both in sulfides and in sodium electrodes. 11,12 In Li-ion batteries, addressing this issue became straightforward by lowering the operating potential. However, in the case of Na-ion batteries, the combination of inherently lower cell potentials and a general dearth of low-voltage, high-capacity anodes presents a further challenge. 6,13,14 Restricting the already limited potential window of Na-ion batteries presents a less optimistic outlook. There is, therefore, a necessity to approach the problem of transition metal migration in Na-ion electrodes to identify methods for preventing these challenges without further limiting the practicality of Na-ion batteries. As in lithium, defects and disorders have been found to improve the performance of Na-ion hosts.<sup>2,6</sup> To this end, amorphous materials offer an alternative that exists at the extreme of disorder and may provide the key to alleviating the detriments of transition metal migration.

Although less popular than crystalline hosts, amorphous structures have shown promise as battery electrodes with some

Received: April 26, 2024
Revised: September 9, 2024
Accepted: September 11, 2024
Published: September 27, 2024





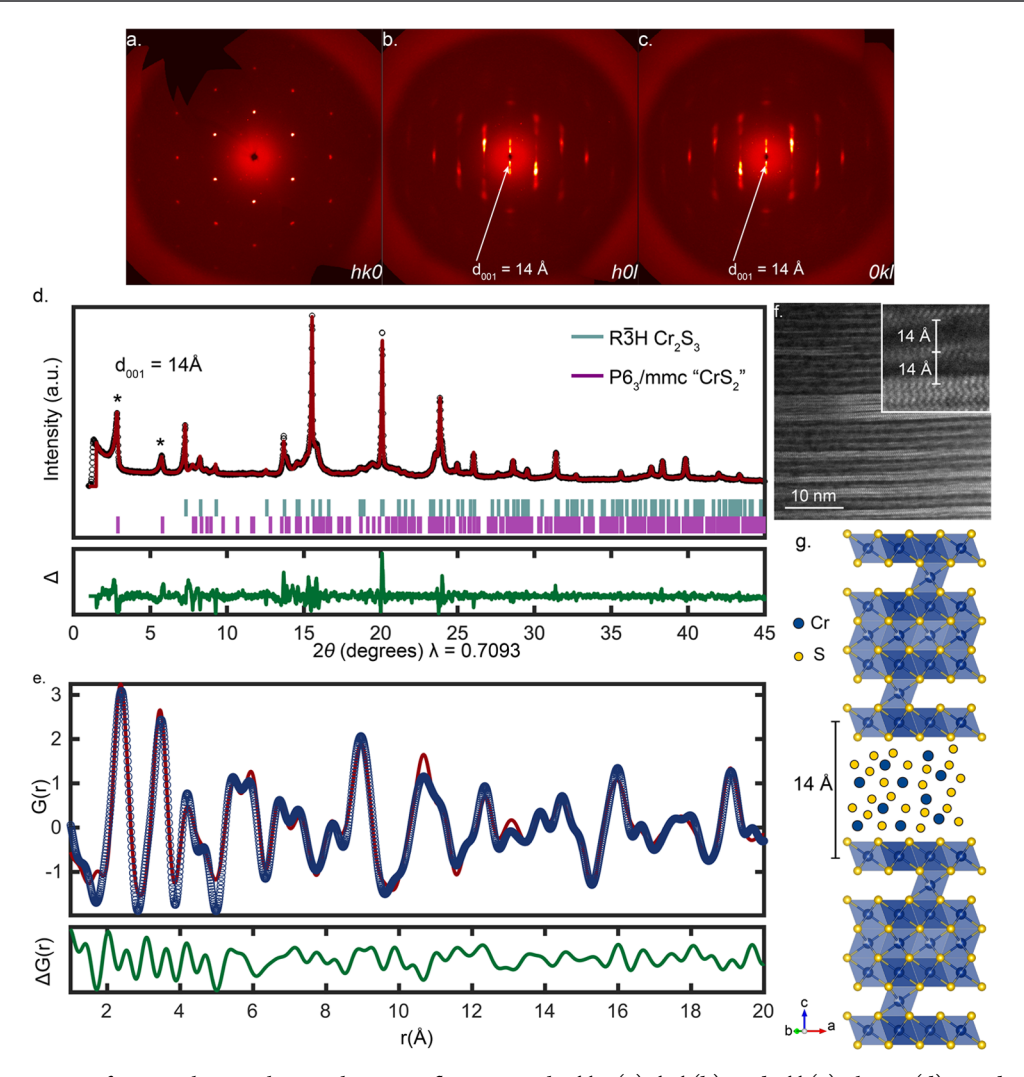


Figure 1. Precession images from single-crystal XRD showing reflections in the hk0 (a), h0l (b), and 0kl (c) planes. (d) Powder XRD data (black circles) with Rietveld refinement for  $Cr_2S_3$  and Pawley fit for a secondary  $(P6_3/mmc)$  phase (red line). Stars indicate peaks due to the slab-to-slab spacing caused by the amorphous intergrowth. (e) Pair distribution function (blue circles) and fitting (red line) of  $H_xCrS_{2-\delta}$  using both a large and small crystallite size to simulate an amorphous phase. (f) Proposed structure of  $H_xCrS_{2-\delta}$ . (g) Cross-sectional STEM image showing the crystalline—amorphous motif in  $H_xCrS_{2-\delta}$  and the amorphous spacing. Inset highlights that the amorphous spacing corresponds to the refined value of 14 Å.

success.<sup>15</sup> Among these, amorphous FePO<sub>4</sub>, V<sub>2</sub>O<sub>5</sub>, other transition metal oxides, and alloys have all demonstrated high capacities with good reversibility.<sup>6,16–18</sup> However, many of these examples undergo amorphization *in situ* and therefore experience significant volume changes during cycling, which result in cracking of the electrode. One solution to the volume change has been through nanocompositing with a mesoporous carbon matrix to allow for expansion.<sup>19</sup> In fact, the majority of amorphous electrodes are composites of the amorphous compound with some other more structurally rigid material to produce an amorphous hybrid.<sup>6</sup> Coupling the amorphous active material with an often inactive crystalline scaffold inherently limits the practical capacity of such hybrid electrodes.

Our group recently reported on a unique "biphasic" structure type found in  $H_x CrS_{2-\delta}$ , which is an intrinsic hybrid compound composed of alternating crystalline and amorphous phases. The parent structure of  $H_x CrS_{2-\delta}$ ,  $NaCrS_2$ , is known to undergo migration of chromium into sodium vacancies on charging, resulting in the aforementioned voltage hysteresis and poor cyclability. Our initial study demon-

strated that the production of a "biphasic" structure can dramatically improve electrode performance but made no speculations about the potential mobility of the transition metal. However, it did seem likely that a more flexible lattice from the amorphous interphase chromium should maintain some of its mobility. In fact, in some cases, a flexible or even mobile lattice has previously been demonstrated to enable ionic motion. <sup>22</sup>

In the initial report of  $H_x CrS_{2-\delta}$ , Song et al. demonstrated that during chemical deintercalation and formation of the amorphous phase, a significant degree of sulfur dimerization takes place. The presence of protons in the material was verified with Raman spectroscopy, which showed a very intense S–H stretching mode. The authors also reported on the compositional differences between the amorphous and crystalline components of  $H_x CrS_{2-\delta}$ , using electron energy loss spectroscopy (EELS) to identify some changes in the coordination of Cr in the amorphous phase. Using scanning transmission electron microscopy-based energy-dispersive X-ray spectroscopy (STEM-EDX), it became visible that the amorphous phase is relatively sulfur-rich compared to the

crystalline phase. Exfoliation of  $H_xCrS_{2-\delta}$  was achieved by shaking in an alkylammonium solution to separate the crystalline layers, resulting in single crystalline nanosheets.<sup>20</sup>

In our report on the electrochemical behavior of  $H_xCrS_{2-\delta}$ , we demonstrated that this new structure promotes fast Na+ diffusion ( $D \approx 10^{-9} \text{ cm}^2/\text{s}$ ), exceeding the diffusivity of Na<sup>+</sup> through NaCrS<sub>2</sub> by over 3 orders of magnitude. We also found that  $H_xCrS_{2-\delta}$  exhibits a high reversible capacity of 728 mAh/ g, whereas NaCrS2 has a reversible capacity of just over 100 mAh/g when used as a Na-ion battery electrode. 11,21 Additionally, we demonstrated that in  $H_xCrS_{2-\delta}$  S, redox is maintained during cycling. By virtue of the high capacity and by some initial spectroscopic evidence, we also found that Cr participates in charge storage and undergoes redox.<sup>21</sup> By contrast, in NaCrS2, only S redox contributes to charge balance during cycling through the formation and breaking of  $(S_2)^{2-}$ dimers. 16 Raman spectroscopy revealed that the protons remain bound to S during discharge. Further, electrochemical evidence showed that it is Na<sup>+</sup> and not H<sup>+</sup> that is responsible for the fast diffusion and high capacity in  $H_xCrS_{2-\delta}$ . The electrochemical behavior of  $H_xCrS_{2-\delta}$  has been summarized in Supplemental Figure S1.

We now present a larger mechanistic exploration of this system to better understand the roles of the amorphous and crystalline lamella and how the structure of each varies during cycling. We used X-ray diffraction and electron microscopy to investigate the structure of annealed  $H_xCrS_{2-\delta}$ . We then probe the structure during electrochemical cycling through a number of ex situ techniques, including X-ray absorption spectroscopy, X-ray diffraction, X-ray total scattering, and magnetometry. We find that the crystalline phase of  $H_xCrS_{2-\delta}$  adopts a defective Cr<sub>2</sub>S<sub>3</sub> structure and that the amorphous phase has a regular 14 Å size separating the crystalline lamella. We find, using magnetometry, strong evidence of Cr redox during cycling. This is further supported by probing the local structure of Cr, which also identifies significant changes in the geometric coordination. Additionally, we find that during discharge,  $H_xCrS_{2-\delta}$  undergoes significant amorphization that is partially reversed on subsequent charging. Lastly, in tandem with our previously reported electrochemical cycling, we present further evidence through galvanostatic titration that H<sub>x</sub>CrS<sub>2-\delta</sub> undergoes significantly less polarization and voltage hysteresis while supporting high capacities and fast ionic diffusion over a wide potential window.

## ■ RESULTS AND DISCUSSION

**Atomic and Electronic Structure.** In our initial report of  $H_xCrS_{2-\delta}$ , the samples were studied directly after proton exchange; we found that annealing the powder or crystals at 150 °C improves the electrochemistry and slightly alters the structure. <sup>20,21</sup> Our previous studies on  $H_xCrS_{2-\delta}$  discussed the alternating structure and presence of protons and included some analysis of the composition and structure.<sup>20</sup> We demonstrated through X-ray photoelectron spectroscopy (XPS) and Raman spectroscopy that an S-H stretch was present in  $H_xCrS_{2-\delta}$ . We also found that the amorphous phase is significantly more sulfur-rich than the crystalline phase. In unannealed samples, the spacing of the amorphous layer was found to be fairly irregular using high-angle annular dark field scanning transmission electron microscopy (HAADF-STEM).<sup>20</sup> We now present a full analysis of the annealed structure. While it is difficult to probe amorphous materials using X-ray diffraction (XRD), it is still a powerful technique to

identify the structure of the crystalline phase of  $H_xCrS_{2-\delta}$ . In Figure 1a–c, single-crystal XRD data are presented, along with powder XRD in Figure 1d, pair distribution function analysis (PDF) in Figure 1e, and STEM imaging in Figure 1f.

Initial Rietveld refinements against powder diffraction data showed little promise for a full structural solution. Most of the peaks in the pattern are readily indexed to the structure of Cr<sub>2</sub>S<sub>3</sub>, but there is still a clear mismatch between the pattern and the refinement. In particular, two peaks (indicated by stars in Figure 1d and Supplemental Figure S2) at 2.78 and 5.70 $^{\circ}$  2 $\theta$ continuously eluded rigorous fitting despite trying numerous space groups. Performing a Rietveld refinement while disregarding these two low-angle peaks results in Cr deficient Cr<sub>2</sub>S<sub>3</sub> (R 3H) with a fractional occupancy on one of the Cr atoms. A fit to the data with only one phase is shown in Supplemental Figure S2 and shows that the single phase is insufficient. However, by adding a second phase  $(P6_3/mmc)$ with an artificially large interstitial gap, we are able to identify the two low-angle peaks corresponding to the amorphous spacing between crystalline slabs. The fit of both phases to the experimental data is shown in Figure 1d, with the peaks for each phase labeled. The P6<sub>3</sub>/mmc phase is fit with a Pawley fit since its amorphous nature prevents a conclusive structure from being solved. Furthermore, this second phase is used to model the slab-slab distance, which is somewhat variable.

Due to the large degree of disorder in  $H_xCrS_{2-\delta}$  and relatively large thermal displacements, any refined formula is unlikely to be completely correct, so we will continue to refer to the material as  $H_xCrS_{2-\delta}$ . Additionally, the biphasic nature somewhat complicates attempts to characterize the composition of the crystalline phase. Song et al. showed that the two phases have different compositions, with the amorphous being richer in S than the crystalline. EDX data and inductively coupled plasma optical emission spectroscopy (ICP-OES) both show an average Cr:S ratio of about 0.52 (Supplemental Figure S5 and Supporting Information Table S5), which is lower than the ratio obtained from Rietveld refinement. This may also be due to the previously reported lower S content observed in the crystalline phase.  $^{20}$ 

Single-crystal XRD reveals that the crystal is well ordered within the a-b plane (Figure 1a), and all disorder comes from increased spacing due to amorphous interlayer lamella in the c direction. This is to be expected, as the amorphous phase interrupts periodicity along that axis and causes the streaking seen in Figure 1b,c. In order to account for the two peaks at 2.78 and 5.70°, we conducted a Pawley fit against powder XRD data using a second phase (P63/mmc) to represent the interstitial spacing; this also resulted in a 14 Å spacing and can be seen in Figure 1d. Adding this second phase decreases the Rwp from 20.11 to 4.28% by fitting the initial two peaks as well as accounts for some peak broadening throughout the pattern as tabulated in Supplemental Tables S1 and S2. That being said, we do not intend for this to be viewed as an actual second phase but are merely using it as a tool to model the large interstitial space containing amorphous material.

In addition to XRD, we employ PDF to investigate the disorder present in  $H_x Cr S_{2-\delta}$ . Figure 1e shows the best fit, which was obtained using both a  $Cr_2S_3$  phase and a nanosized  $Cr_2S_3$  phase to simulate an amorphous component. Additionally, the best fit was obtained by allowing anisotropic displacement values with an extremely large  $U_{33}$ , indicating disorder along the *c*-axis in the stacking direction in agreement with the single-crystal XRD.<sup>23</sup> Demonstrations of fits without

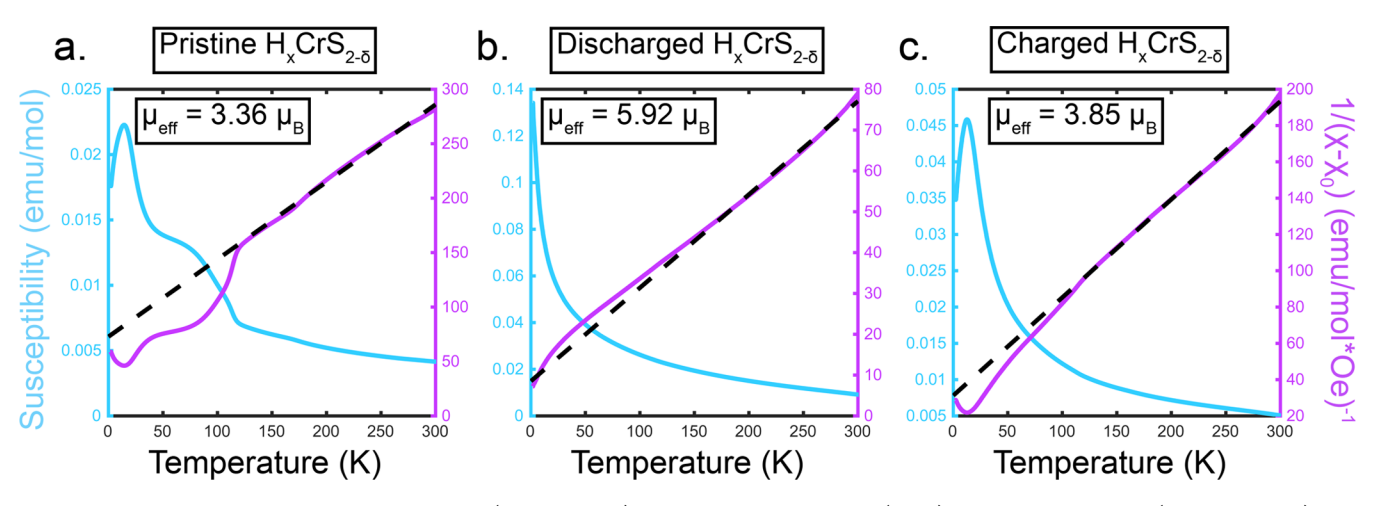


Figure 2. ZFC susceptibility vs temperature plots (blue, left axis) measured at 1000 Oe,  $1/(\chi-\chi_0)$  vs temperature plots (pink, right axis), and associated Curie–Weiss fits (dashed black line) with the 150 to 300 K regions of (a) pristine  $H_x CrS_{2-\delta}$ , (b)  $H_x CrS_{2-\delta}$  discharged to 0.1 V, and (c)  $H_x CrS_{2-\delta}$  discharged to 0.1 V and subsequently charged to 3 V demonstrate the reversible Cr redox of  $H_x CrS_{2-\delta}$ . A small  $\chi_0$  value was subtracted from each fit to account for the effects of impurities and additives.

this amorphous component or with isotropic displacement are shown in Supplemental Figure S3 and the fitted parameters for the fits are shown in Supplemental Table S4.

Comparing the unit cell obtained from single-crystal data with the structure determined from powder diffraction and scanning transmission electron microscopy (STEM) images indicates that the starred peaks may be attributed to increased spacing in the c direction caused by the amorphous layers. The low-angle peaks in both single-crystal (Figure 1b and c) and powder data (Figure 1d) agree with a d-spacing of 14 Å. This distance is measurable in TEM, in which a lattice fringe is visible in crystalline regions, and an incoherent region between the crystalline slabs indicates the amorphous layer. The inset in Figure 1g shows the same 14 Å separation between crystalline slabs that is determined from XRD. High-resolution STEM (HRSTEM) imaging of  $H_xCrS_{2-\delta}$  at a variety of magnifications in Supplemental Figure S4 reveals the alternating layers in  $H_rCrS_{2-\delta}$ , which are reminiscent of lamellar block copolymers, although admittedly somewhat more ordered and with much thinner lamella.<sup>24</sup> HRSTEM images additionally show that the spacing is significantly more regular after annealing.<sup>20</sup> This marks a significant difference between annealed and unannealed  $H_x Cr S_{2-\delta}$ . As shown by Song et al., before annealing, the structure more closely resembles a disordered  $Cr_{1-xS}$ , and the size of the amorphous phase lacks the regularity we report here. In our group's initial report on  $H_xCrS_{2-\delta}$ , we proposed a multistep formation of the crystalline phase in which Cr migrates through the sodium site into an ABA stacking pattern as in both CrS and Cr<sub>2</sub>S<sub>3</sub> that occurs as the sample dries.<sup>20</sup> It is possible that by annealing, this migration is driven further to produce the regularity and crystal structure we present here. These data provide an in-depth understanding of the structure of the crystalline scaffold of  $H_xCrS_{2-\delta}$  and yield the approximate structure shown in Figure 1f, in which the amorphous phase is indicated by randomly spaced Cr and S atoms.

With this new structural description of  $H_x CrS_{2-\delta}$ , it is worth revisiting a fundamental question. There is no literature suggesting that  $Cr_2S_3$  is likely to host sodium to any satisfactory degree. How is it then that  $H_x CrS_{2-\delta}$  exhibits such remarkable performance as a Na<sup>+</sup> host? One potential reason may lie in the electronic structures of NaCrS<sub>2</sub> and

 $H_xCrS_{2-\delta}$ . Since we have modeled the crystalline component of  $H_rCrS_{2-\delta}$  as defective  $Cr_2S_3$  and density functional theory (DFT) is limited in its ability to model nonperiodic systems or fractional occupancy, we here use Cr2S3 as a model for the electronic structure of H<sub>x</sub>CrS<sub>2-δ</sub>. NaCrS<sub>2</sub> exhibits only S redox as it is cycled. This can be explained by the S dominant density of states (DOS) below the Fermi level, as shown in Supplemental Figure S6a. As NaCrS2 is oxidized, electrons must be removed from these S states rather than from Cr. Cr redox is therefore inaccessible before entering the potential window in which transition metal migration takes hold. By contrast, Cr<sub>2</sub>S<sub>3</sub> has a Cr dominant DOS immediately above the Fermi level, where electrons may be added during reductive discharge, as shown in Supplemental Figure S6b. In our group's previous reports on H<sub>x</sub>CrS<sub>2-8</sub>, we have shown the formation of S22- dimers during proton exchange and their reversible cleavage during cycling. <sup>20,21</sup> In conjunction with the Cr<sub>2</sub>S<sub>3</sub> DOS, this may enable Cr redox in addition to S redox in H<sub>x</sub>CrS<sub>2-\delta</sub>, allowing for higher capacities. We note, however, that due to the amorphous interphase and interactions between the two phases, the electronic structure for Cr<sub>2</sub>S<sub>3</sub> is not a perfect model for  $H_xCrS_{2-\delta}$  but rather is a tool to identify potential redox mechanisms.

It seems as though the amorphous phase is crucial to the electrochemical improvements that have been reported. Additionally, the changes in the electronic structure appear to allow additional redox pathways. While  $Cr_2S_3$  is known to limit capacity in Na-ion batteries, it has shown promise in Li systems when paired with a porous carbon structure to alleviate volume expansion-related problems. It is possible that the amorphous interphase of  $H_xCrS_{2-\delta}$  achieves a similar effect. We pursue clarity of the structural and electrochemical mechanisms at play through a combination of magnetometry, X-ray absorption spectroscopy, and electrochemical titration.

**Magnetometry.** We employ magnetometry to quantitatively study changes at the Cr center at the termini of charge and discharge to track changes in the Cr oxidation state. Zerofield-cooled (ZFC) susceptibility vs temperature plots reveal a broad feature reminiscent of the  $\text{Cr}_2\text{S}_3$  ferrimagnetic transition starting just above 100 K in the pristine material, which is consistent with the structure of the crystalline phase of  $H_x\text{CrS}_{2-\delta t}$  as well as an antiferromagnetic transition at about

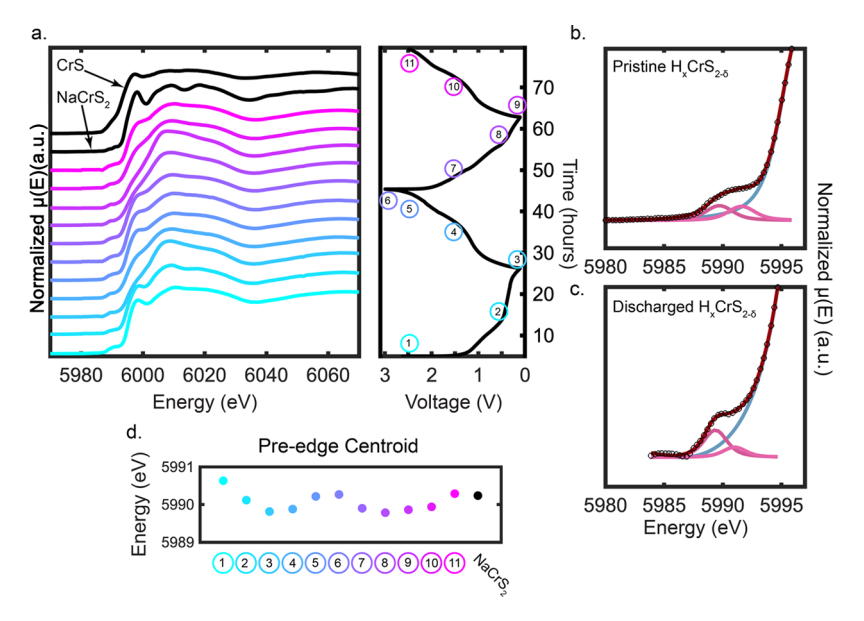


Figure 3. (a) Cr K-edge XANES shows the evolution of the edge structure during charge and discharge of  $H_xCrS_{2-\delta}$  as well as that of CrS and NaCrS<sub>2</sub> (the top and second black lines, respectively) as standards. A typical charge—discharge profile and points at which electrodes were harvested for study by XAS are provided as a legend. The discharge capacity of the cell that produced this data was 619 mAh/g. (b) A representative fit to the pre-edge feature in pristine  $H_xCrS_{2-\delta}$  and discharged  $H_xCrS_{2-\delta}$  (c) in which the blue line is a fitted background, the pink lines are fitted peaks, and the red line is the sum of the fit. (d) The location of the pre-edge fit centroid follows the expected trend for Cr redox during charge and discharge.

14.3 K as seen in Figure 2a.  $^{26}$  The ferrimagnetic transition is more pronounced at lower fields ( $\sim$ 500 Oe) and is shown in Supplemental Figure S7a. After discharge, that magnetic order is largely lost, presenting a mostly featureless paramagnetic response (Figure 2b). Following the subsequent charge, the  $Cr_2S_3$  ferrimagnetic response can still be seen at low fields ( $\sim$ 500 Oe) Supplemental Figure S7c but is mostly invisible at higher fields (1000 Oe), where only the antiferromagnetic transition at 12.5 K is present (Figure 2c). This shows that some of the original crystalline structure is recovered during charging and desodiation, even after near-complete amorphization of the material during discharge.

More quantitative analysis in the form of Curie-Weiss fits can be applied to the magnetometry data (shown by the black dashed lines in Figure 2). The multiphasic nature of the material and the additives needed to operate as an electrode necessitate small  $\chi_0$  subtraction from each sample due to temperature-independent effects on susceptibility.<sup>27</sup> In pristine  $H_xCrS_{2-\delta}$ , a  $\mu_{eff}$  of 3.36  $\mu_B$  is found, corresponding well with previously reported values.<sup>20</sup> This also coincides with the expected spin-only moment for a nearly perfect 1:1 ratio of  $Cr^{3+}:Cr^{4+}$  ( $d^3:d^2$ ), in agreement with previous reports on  $H_xCrS_{2-\delta}$ . After discharge,  $\mu_{eff}$  increases to 5.92  $\mu_B$ , corresponding well with that for high spin Cr1+ (d5), which confirms the expectation that Cr must participate in redox to achieve the measured capacity of 728 mAh/g.<sup>21</sup> Measurements of samples that had been discharged and then charged show a  $\mu_{eff}$  of 3.85  $\mu_{B}$ , indicating that at least 2 out of the 3 electrons required to achieve that capacity come from reversible Cr redox. Curie-Weiss fits reveal not only that Cr is redox-active but that in  $H_rCrS_{2-\delta}$ , Cr undergoes two-electron redox as expected, given the high observed capacity. Additionally, we see that further sodiation is limited, at least in part, due to the spin pairing energy barrier that would need to be overcome in order to further reduce to Cr metal. While Cr<sup>1+</sup> is rare, it is not without a literature precedent. In fact, Cr<sup>1+</sup> has been identified

in  $CrF_2$ , in linear chain lattices, and in redox-active systems such as chromium phthalocyanine, in which a  $Cr^{3+}$  enter can be reduced to  $Cr^{1+}$  and further reduction results in demetalation.

X-ray Absorption Spectroscopy. X-ray absorption fine structure spectroscopy (XAS) and its subclasses (extended X-ray absorption fine structure (EXAFS) and X-ray absorption near edge spectroscopy (XANES)) are powerful techniques for probing the aggregate local coordination and oxidation states of specific elements. We employ Cr K-edge XAS to study changes in the environment of Cr atoms at various states of charge indicated along the charge—discharge curve in Figure 3b. Ex situ spectra were collected over the course of two full cycles to ensure that any changes seen were reversible and not simply due to initial rearrangements or surface-electrolyte interphase (SEI) formation during the first discharge.

The XANES region (Figure 3a) demonstrates a clear change in the qualitative shape of the rising edge and its surrounding area, indicating possible changes in the ligand geometry. The edge position, usually defined as either the first peak of the derivative or the position of half-maximum intensity, is convoluted by shakeup/shakedown processes, as shown in Supplemental Figure S8, and is therefore not useful for identifying Cr oxidation states. 31,32 This is discussed further in the Supporting Information. However, a trend can still be identified in the pre-edge, supporting Cr redox. While a 1s  $\rightarrow$ 3d pre-edge peak is formally "forbidden" in octahedral geometry, a weak response is still often observed experimentally.<sup>33</sup> In our Cr XAS experiments, we see this weak peak appearing before the edge and perform fitting, examples of which are shown in Figure 3b and c. By fitting this pre-edge feature, we are able to identify that the intensity weighted average position (centroid) of the pre-edge follows the expected trend for Cr redox in this system, that is, decreasing in energy during discharge and increasing during charging, as shown in Figure 3d. Formally, multiplet analysis is necessary to

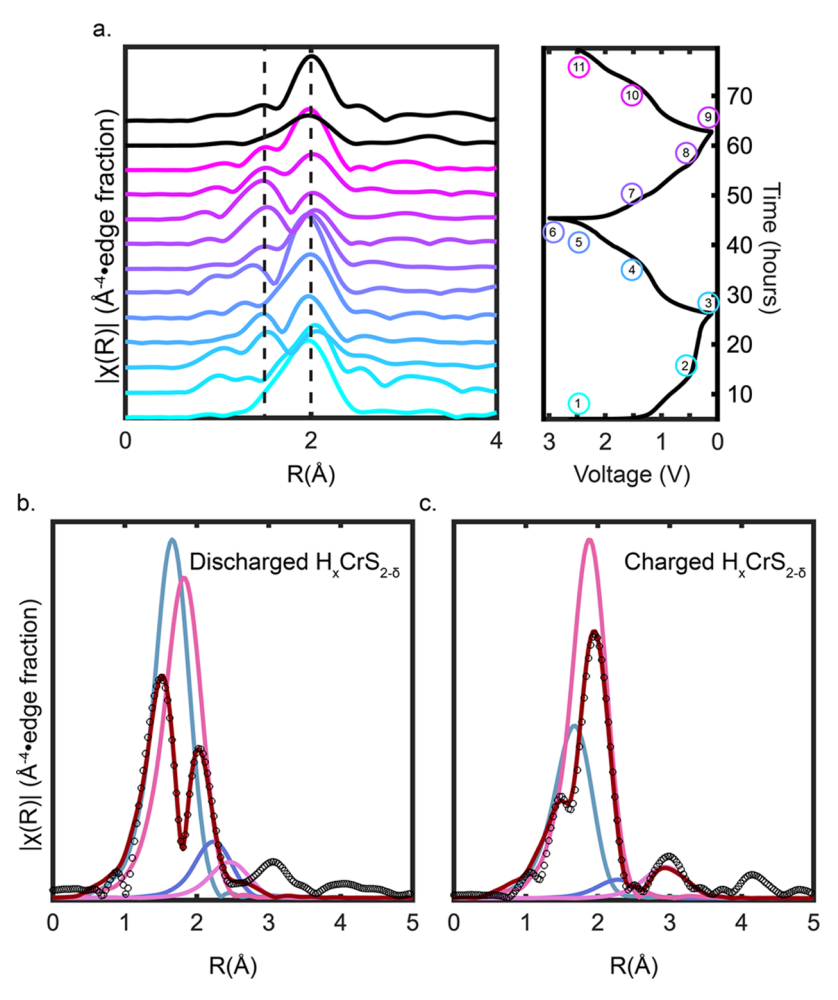


Figure 4. Cr K-edge EXAFS radial distribution (a) shows the evolution of the first coordination shell as a function of the charge and discharge of  $H_xCrS_{2-\delta}$ . A typical charge—discharge profile and points at which electrodes were harvested for study by XAS are provided as a legend. (b) Example fit of discharged  $H_xCrS_{2-\delta}$  and (c) example fit of charged  $H_xCrS_{2-\delta}$  illustrate the lower bond distance that grows during discharge.

fully characterize the excited electronic state in this pre-edge. A discussion of multiplet analysis and why it cannot be employed in this study is provided in the SI. By fitting with two peaks, we can identify that the effective nuclear charge changes as a function of charge and discharge as indicated by the centroid position. The decreasing energy of the pre-edge during discharge makes clear that Cr reduction occurs, as determined from magnetometry, and that it is reversible as the pre-edge recovers to a higher energy during charging. This result supports those of our magnetometry experiments and indicates a strong likelihood of Cr redox in this system. A further explanation of this analysis and all fits to the pre-edge are provided in the SI and Supplemental Figure S9.34 As the preedge peaks remain quite small during cycling, little can be inferred from these data about the coordination of Cr. Therefore, it is necessary to consider the EXAFS region.

To pursue the geometric changes suggested by the edge position and shape, we turn to the radial distribution (Figure 4a), which shows a contraction of the first coordination shell bond length during discharge. The two bond lengths are indicated by dashed vertical lines to guide the eye. This is somewhat unexpected as the reductive environment of discharge would ordinarily cause the bond to relax. However, thorough characterization by fitting the EXAFS region can reveal clearer information about these changes. While six-coordinate Cr fits well to the pristine  $H_xCrS_{2-\delta t}$  the EXAFS fits

suggest that the inclusion of four-coordinate Cr is more plausible and necessary to fit the discharged samples (Figure 4b). Figure 4c illustrates that subsequent charging results in a diminishing of this four-coordinate Cr, indicating a reversible change in the coordination of Cr during cycling. Fits shown in Supplemental Figures S10–S13 show that this additional Cr site can be fit by either a shortening of the Cr–S bond and concurrent change in coordination number from 6 to 4 or by a similarly four-coordinate Cr–O bond. All data was fit using both models and are compared in Supplemental Tables S6–S11.

The model, including two Cr-S paths corresponding to a 6-coordinate and a 4-coordinate Cr, fit the data better in 4 out of 10 data sets, namely, the first discharge at 0.5 V and 0.1 V, the first charge at 2.5 V, and the second charge at 2.5 V. The model with one 6-coordinate Cr-S path and one 4-coordinate Cr-O path fit slightly better in 5 out of 10 data sets, those being the first charge at 1.5 V, the second discharge at 1.5, 0.5, and 0.1 V, and the second charge at 1.5 V. In the first discharge at 3 V, the Cr-O model exhibits a marginally better fit. We will discuss here two potential explanations of the data, one of which is supported by the model with two Cr-S paths and the other by the model with one Cr-S and one Cr-O path. However, in both cases, it is clear that Cr must move into and subsequently back out of a 4-coordinate environment and, therefore, demonstrative that the migration of Cr is not

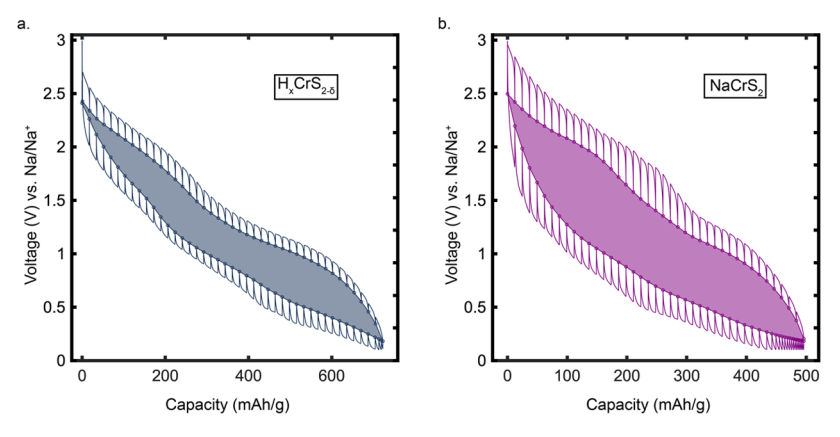


**Figure 5.** Galvanostatic intermittent titration identifies both a smaller voltage hysteresis and lower polarization in  $H_xCrS_{2-\delta}$  (a) than that in NaCrS<sub>2</sub> (b).

hindered in  $H_x Cr S_{2-\delta}$  despite measurable improvements in electrochemical performance.

In the case of Cr-O bond formation, there are several possibilities that must be ruled out. First, exposure to air could result in the formation of Cr<sub>2</sub>O<sub>3</sub>. However, the samples were treated in the same manner as those for magnetometry and for ex situ XRD (Supplemental Figure S14), neither of which indicates evidence of Cr<sub>2</sub>O<sub>3</sub>. Additionally, in Cr<sub>2</sub>O<sub>3</sub>, Cr is coordinated to 6 O atoms, and the inclusion of a six-coordinate Cr-O path in fitting was unsuccessful in all cases. Therefore, exposure to the atmosphere does not fit with the data and is unlikely. Second, the electrolyte solvent is an ether (diglyme) and so could feasibly cleave and react with the low valent Cr atoms in the electrode. However, this would certainly appear in the electrochemical data, and no such electrolyte decomposition was observed. There has been some literature that suggests diglyme can act as a tridentate ligand of Cr in which each O atom of the diglyme is bound to the Cr center.<sup>36</sup> Additionally, organic ligands, particularly alkyl amino carbenes, have been demonstrated to stabilize Cr(I).<sup>37</sup> This may indicate that the organic solvent plays a role in facilitating the migration of Cr during the cycling of  $H_xCrS_{2-\delta}$  and assists in stabilizing the low oxidation state at deep discharge. However, the reversibility of the Cr movement similarly suggests that this explanation too is incorrect, as the dissolution of Cr into the electrolyte would likely result in a significant loss of capacity as active material is lost. It is therefore useful to consider the alternative, a model with only Cr-S paths.

In the model with only Cr-S pathways, the second pathway is similarly shortened and 4-coordinate. Such geometries include both tetrahedral and square planar. Each octahedron in the crystalline structure shares a face with a tetrahedral vacancy, so the Cr atom could, in principle, migrate through it. Another possibility may be a distortion of the Cr-S octahedra, resulting in a formal square planar geometry for Cr. This could occur if the fully occupied Cr-S layers migrated in opposite directions parallel to the a-b plane. It should, however, be noted that XAS is not limited to the response from the crystalline phase, so it is also possible that the change in coordination is indicative of a further amorphization of the structure during discharge, resulting in 4-coordinate molecular or polymeric CrS<sub>4</sub> species, perhaps related to amorphous CrS<sub>3</sub>. 38,39 In fact, ex situ XRD (Supplemental Figure S14) demonstrates that as  $H_xCrS_{2-\delta}$  is discharged, it undergoes significant amorphization, and some peaks (albeit incredibly broad) return on subsequent charging. This suggests that

rather than any coherent migration of the Cr during discharge, loss of crystalline Cr to the amorphous phase is likely responsible for the change in coordination number. This seems to be the more plausible explanation of all of the data as it is supported not just by the XAS but also by XRD and magnetic susceptibility measurements.

In both models, it is evident that the Cr migration is persistent during cycling. Additionally, in neither case was fitting with exclusively 6-coordinate Cr successful, indicating a necessary decrease to a 4-coordinate environment. Representative fits of discharged and charged  $H_x CrS_{2-\delta}$  are shown in Figure 4 c and d, illustrating these geometric changes during cycling.

This introduces a curious result. Despite improved electrochemical performance, Cr migration still occurs and, in fact, appears to be nearly completely unhindered. Since this is the source of capacity fade in NaCrS<sub>2</sub>, it at first seems odd that such motion should not elicit the same issues in  $H_x \text{CrS}_{2-\delta}$ . However, it could be that Cr in the amorphous phase has a lower barrier to migration, allowing smaller overpotentials in  $H_x \text{CrS}_{2-\delta}$  than those seen in its counterpart. Additionally, the pliability of the amorphous phase likely allows for the diffusion of Na<sup>+</sup> ions through the structure despite the motion of the transition metal, whereas a more rigid structure might collapse as a result of Cr migration and trap the Na<sup>+</sup>. The result of all this is that the introduction of the biphasic structure of  $H_x \text{CrS}_{2-\delta}$  allows for reversibility within a larger operating regime, which enables higher capacity.

Galvanostatic Intermittent Titration Technique. Our previous report on  $H_xCrS_{2-\delta}$  used the galvanostatic intermittent titration technique (GITT) to confirm the fast diffusivity of Na<sup>+</sup> through the material.<sup>21</sup> In this study, GITT is used to identify polarization during the cycling of both  $H_xCrS_{2-\delta}$  and NaCrS<sub>2</sub>. GITT utilizes a brief constant current pulse followed by a long relaxation to measure equilibrium potentials during cycling. This also affords the opportunity to measure polarization, as identified by the magnitude of the relaxation curve. Previous studies on transition metal migration have demonstrated lower polarizations with the introduction of defects in the active material crystal structure. Our previous work on  $H_rCrS_{2-\delta}$  shows that the charge and discharge curves of  $H_xCrS_{2-\delta}$  operate at far more similar potentials than those of NaCrS2, so it can be expected that polarizations will be lower.<sup>21</sup> GITT was performed on both H<sub>x</sub>CrS<sub>2-δ</sub> and NaCrS<sub>2</sub> (Figure 5a and b, respectively) and as predicted, we see lower polarization in  $H_xCrS_{2-\delta}$  than in its precursor. As noted in the

previous literature, we see a decrease in voltage hysteresis as well. This provides further evidence that the formation of biphasic  $H_x CrS_{2-\delta}$  and the mechanistic and structural changes that come with it enables superior performance compared to NaCrS<sub>2</sub>. With  $H_x CrS_{2-\delta}$  as a model system, this demonstrates the capabilities of biphasic structures to improve the existing canon of energy storage materials.

**Conclusions.** Our results demonstrate that the biphasic material  $H_x CrS_{2-\delta}$  enables high performance through a complex interplay of structural and electronic reorganization. Through XRD and TEM, we presented here a rigorous structural description of  $H_x CrS_{2-\delta}$ . XRD and PDF positively identify the crystalline structure as  $Cr_2S_3$  after annealing, while the techniques agree that the amorphous gap in the material is consistently  $\sim 14$  Å. DOS of  $Cr_2S_3$  and  $NaCrS_2$  are compared to identify possible reasons for the differences in their electrochemical behavior. The presence of Cr dominant states immediately above the Fermi level in  $Cr_2S_3$  provides an explanation for the observed reversible Cr redox in  $H_x CrS_{2-\delta}$  that is absent in  $NaCrS_2$ .

Ex situ magnetometry measurements and the shifts in edge position in XANES provide substantial evidence of reduction from  $Cr^{3+}/Cr^{4+}$  to  $Cr^{1+}$  during discharge and demonstrate that this reduction is reversibly reoxidized on charging. In conjunction with our previous demonstration that S redox persists in  $H_xCrS_{2-\delta}$ , this provides reasonable proof of both cationic and anionic redox during cycling. Rigorous fitting of EXAFS data additionally reveals that during discharge, Cr moves from a 6-coordinate site into a 4-coordinate site. In tandem with the amorphization seen in ex situ XRD, this indicates that as Cr moves out of the crystal lattice during discharge, it also undergoes changes in coordination number and ligand geometry.

Despite apparent transition metal migration, GITT measurements and our previous report demonstrate that the electrochemical behavior of  $H_x Cr S_{2-\delta}$  does not suffer from the effects of migration that are typically seen in layered crystalline materials. This appears to be in large part due to the inclusion of an amorphous layer between  $Cr_2S_3$  lamella providing a pliable medium in which  $Na^+$  can diffuse readily. Simultaneously, the crystalline scaffold of  $H_x Cr S_{2-\delta}$  appears to provide stability to the electrode, which allows for better cycling behavior than bare amorphous structures.

This work investigates the interplay of Cr redox and dynamics during the electrochemical cycling of an intrinsically biphasic material. In particular, we have demonstrated, through  $H_x CrS_{2-\delta}$ , the potential of biphasics to improve the capabilities of materials in which transition metal migration is the leading limitation to capacity. This is accomplished not through freezing the transition metal but rather through a complex interaction at the interface of the amorphous phase and its crystalline scaffold. This novel structural motif enables the usage of amorphous electrodes within a compositionally matched lattice scaffold that supports it and allows for better reversible cycling. Biphasic structures offer a new system in which to study transport and redox phenomena that may reveal a wealth of new energy storage materials.

#### EXPERIMENTAL SECTION

**Materials Synthesis.** NaCrS<sub>2</sub> powder was prepared by solid-state reaction of Cr powder ( $\sim$ 100 mesh 99% metals basis, Alfa Aesar), Na<sub>2S</sub>, and S powder ( $\sim$ 100 mesh 99.5%, Alfa Aesar) in a 1:2:10 molar ratio. After grinding with an agate mortar and pestle, the mixture was

transferred to an alumina crucible sealed in a fused silica tube under vacuum (65–75 mTorr) that had been flushed with Ar. The powders were heated to 700 °C at 2 °C per minute and held at temperature for 48 h before being allowed to cool to room temperature. Powders were washed with DI water and ethanol before characterization or use as electrodes. Single crystals of NaCrS $_2$  were produced according to the synthesis by Song et al.  $^{20}$  The same Cr, Na $_2$ S, and S powders were combined in a 1:3:4 molar ratio. After similar grinding, the powder was sealed in an alumina crucible in a fused silica tube under a vacuum. The powder was heated to 1000 °C at 2 °C per minute, held at this temperature for 24 h, and then cooled to 300 °C at a rate of 25 °C per hour. Single crystals with a lateral size of ~5 mm were harvested and washed with DI water and ethanol before proton exchange, as described below.

 $\rm H_x Cr S_{2-\delta}$  was produced from NaCrS $_2$  according to our previously reported proton exchange method.  $^{20,21}$  Powders or crystals were shaken in a 1 M solution of HCl in 25% DI water in ethanol for 4 days, exchanging the solution every day. After proton exchange, samples were washed with DI water and ethanol before being transferred to an alumina crucible in a fused silica tube, flushed with Ar, and sealed under a vacuum. The sample was then annealed at 150 °C for 72 h. As a safety precaution, ampules were opened in a fume hood due to the potential production of  $\rm H_2S$  during annealing. After being annealed, powders were ground and prepared for characterization or use as electrodes. Single crystals were picked and used for STEM or single-crystal XRD preparation.

**X-ray Diffraction.** Powder XRD patterns were collected using a STOE STADI P diffractometer with a monochromated Mo source ( $\lambda_{Ka1} = 0.7093$  Å). Ex situ patterns were collected by harvesting electrodes after either the first discharge or the first full discharge/charge cycle. The pristine pattern was refined using TOPAS V7 (Bruker AXS). 41,42

Small-single crystals were picked for single-crystal X-ray diffraction analysis using an APEX2 CCD diffractometer equipped with a Mo ( $\lambda_{K\alpha 1}=0.7093\,$  Å) sealed-tube X-ray source and graphite monochromator at 300 K. Indexation was completed for a full hemisphere collection to a resolution of 0.5 Å. Run list generation and frame data processing were done in APEX2.

**Pair Distribution Function Analysis.** The diffraction patterns for PDF analysis were collected over a range of Q=0.2 to 15.8 Å<sup>-1</sup> on a STOE STADI P diffractometer with a monochromated Mo X-ray source ( $\lambda_{K\alpha 1}=0.7093$  Å), with an exposure time of 35 s and a PSD step of 0.03°. The powder samples were contained in Lindeman capillaries with a 0.3 mm diameter that had been flame-sealed. An empty Lindemann capillary was measured by using the same instrument settings for background subtraction. PDFs were produced using the PDFgetX3 software with a Qmax = 12.1 Å<sup>-1</sup> and an r-poly value of 1.0. <sup>44</sup> PDFgui v2.0 was employed for structural refinement in real space. <sup>45</sup> Refined variables included scale factor (s), lattice parameters a and c, quadratic coefficient δ2, and the isotropic thermal displacement parameters (U<sub>11i</sub> U<sub>22i</sub>, and U<sub>33i</sub>), which were assumed to be element specific. <sup>45</sup> Instrument parameters were derived by using LaB<sub>6</sub> as a calibrant.

**Electron Microscopy.** Thin lamella was prepared for STEM imaging by using a Helios NanoLab G3 UC dual-beam focused ion beam and scanning electron microscope (FIB/SEM) system. Single crystals of  $H_x$ CrS $_{2-\delta}$  were prepared, and a flake measuring  $\sim 20~\mu m$  by 15  $\mu m$  was cut and thinned to a thickness of  $\sim 50~nm$ . Sample thinning was accomplished by gently polishing the sample using a 2 kV Ga<sup>+</sup> ion beam in order to minimize surface damage caused by the ion beam.

Atomic resolution HAADF-STEM imaging and EDX mapping were performed on a Titan Cubed Themis 300 double Cs-corrected scanning/transmission electron microscope (S/TEM) equipped with an extreme field emission gun source and a super-X EDS system. The system was operated at a voltage of 300 kV.

**Density Functional Theory Calculations.** Density functional theory (DFT) calculations were performed using Vienna Ab initio Simulation Package (VASP)  $6.3.1.^{46,47}$  Spin-polarized calculations for both the parent compound and  $H_x CrS_{2-\delta}$  were conducted with

Perdew–Burke–Ernzerhof (PBE) functional for exchange–correlation and recommended projector augmented wave (PAW) potentials for all atoms. For the Ueff value is set to 3.5 eV according to previous studies. The size of a  $\Gamma$ -centered Monkhorst–Pack mesh was increased until the convergence was reached. Calculations on NaCrS2 performed on experimental geometry are reported in the Inorganic Crystal Structure Database without additional relaxation. Similarly, the calculation on  $H_x CrS_{2-\delta}$  was performed on the experimental structure parameters without additional relaxation.

Magnetometry. Magnetometry measurements were carried out in a SQUID-VSM magnetic property measurement system (MPMS3: Quantum Design). Samples were kept air-free in an Ar atmosphere glovebox, and powder holders for the MPMS were kept air-free by sealing them with GE varnish and Teflon tape under Ar. M vs T measurements were done from 2 to 300 K at 500 and 1000 Oe. Elemental compositions of the *ex situ* samples were obtained from EDX, as summarized in Supplemental Figure S15 and Supplemental Table S12.

X-ray Absorption Spectroscopy. XAS spectra were collected at the Cr K-edge from about 150 eV below the edge at 5850 eV up to about 900 eV above the edge at 6930 eV. In the XANES region, the step size was 0.3 eV; beyond the XANES, up to 130 eV past the edge, the step size was 1 eV, and beyond that was 2 eV. Ex situ collection points were chosen based on the voltage profile, and electrodes were harvested during both the first and second cycles. Spectra were collected at 0.5 and 0.1 V in the first discharge, 1.5, 2.5, and 3 V in the first charge, 1.5, 0.5, and 0.1 V in the second discharge, and 1.5 and 2.5 V in the second discharge. These cells had a typical capacity of about 620 mAh/g. Additionally, spectra were collected for pristine  $H_xCrS_{2-\delta}$  and NaCrS<sub>2</sub> as well as CrS for comparison. Samples were first cycled to each point of interest in a coin cell before being harvested and washed with fresh diglyme to clean off excess electrolytes and then washed again with hexane before mixing with BN to dilute the material for XAS. All spectra were collected at the Cornell High-Energy Synchrotron Source at the PIPOXS beamline (2A) in transmission geometry with a Si (111) monochromator. Harmonic rejection and focusing of the incident beam were achieved using a pair of focusing mirrors upstream of the sample set to 4 mrad, providing a beam size of 1 mm by 1 mm at the sample. Beam intensity before and after the sample was recorded using N2-filled ion chambers, and the incident energy was calibrated using the first inflection point of an in-line Cr foil (5989.0 eV). The samples were maintained at room temperature and held under vacuum throughout the measurement. The raw data contained systematic glitches at 6726, 6510, 6630, and 6330 eV, at which energies a single data point caused nonphysical spectra in k-space. These individual data points were removed manually. Since these occurred in all spectra and were present in the incident beam, we assign them as monochromator glitches that are not representative of actual physical phenomena.

EXAFS data was processed and fit using XAS Viewer in the X-ray Larch software package. <sup>54</sup> The spectra were normalized and weighted by  $k^3$  before the Fourier transform to the R space for EXAFS analysis. For the Fourier transform, a k-window from k = 2 to k = 12 and fitted data used a Hanning window from R = 1 Å to R = 3 Å. Fitted parameters are shown in Supplemental Tables S6–S11, and the fitted spectra are shown in Supplemental Figures S10–S13.

XAS Viewer was also used to fit the pre-edge using a Linear+Voigt background to accommodate the rising edge and two Voigt peaks in the pre-edge itself. The fwhm of the two peaks were fixed to each other as was done by Westre et al.<sup>33</sup> Fits were visually inspected to ensure that no additional features contributed to the fitted peaks. All fits are shown in Supplemental Figure S9.

**Electrochemistry.** Electrodes were prepared differently according to each need of the characterization technique. For *ex situ* XAS experiments and GITT,  $H_x CrS_{2-\delta}$  was mixed with carboxymethyl cellulose (CMC) and SuperP Carbon C-65 in an 80:10:10 ratio by weight and cast on the copper foil as a water-based slurry. Electrodes with a diameter of 7/16 in. were then punched out and used in CR2032 coin cells. The electrodes had a typical active mass between 2 and 4 mg/cm². The electrolyte was 0.5 M NaPF<sub>6</sub> in bis(2-

methoxyethyl) ether (diglyme), and Celgard 2320 separators were used. For ex situ XRD and magnetometry, a larger mass was necessary, so pellet electrodes were used.  $H_x Cr S_{2-\delta}$  was mixed with polytetrafluoroethylene (PTFE) and SuperP Carbon C-65 in an 80:10:10 weight ratio and pressed into 1/2 in. diameter pellets with a typical mass of around 30 mg. Since PTFE is etched by Na salts in diglyme, NaClO<sub>4</sub> in 1:1 ethylene carbonate/dimethyl carbonate was used as the electrolyte. Start A glass fiber separator was used for these experiments.

The counter electrode in all cells was sodium metal that had been rolled out to a thickness of about 100  $\mu$ m. Coin cells were cycled on a Biologic BCS-805 battery cycler at a rate of C/20 to the intended point and then held at that potential to ensure equilibrium and to prevent self-discharge or equilibration to an unknown potential before electrodes were harvested. Each electrode was washed with diglyme and hexanes to remove any remaining electrolytes. This process also dispersed the electrode powder in hexane, after which the dispersion could be centrifuged to recover the powder for subsequent characterization.

GITT experiments were carried out with the same cell construction as for XAS on a Biologic SP-150 potentiostat using a 30 min current pulse at an equivalent current to a rate of C/20 followed by a 2 h relaxation in a potential window from 0.1 to 3 V. GITT was measured on the second discharge—charge cycle to avoid any formation effects at the anode during the first cycle. The total charge passed through the electrode was limited to the theoretical capacity in order to trigger the next step in the experiment. NaCrS $_2$  cells were prepared in the exact same way as  $\rm H_xCrS_{2-\delta}$  using the same additives at the same ratios as well as the same electrolyte and cycling parameters.

#### ASSOCIATED CONTENT

## Supporting Information

The Supporting Information is available free of charge at https://pubs.acs.org/doi/10.1021/acs.chemmater.4c01232.

Additional XRD analysis; PDF analysis; TEM data; EDX data; DOS calculations; XAS fits and fitting details; *ex situ* XRD; and additional magnetic data at low field (PDF)

# AUTHOR INFORMATION

# **Corresponding Author**

Leslie M. Schoop — Department of Chemistry, Princeton University, Princeton, New Jersey 08540, United States; Princeton Materials Institute, Princeton University, Princeton, New Jersey 08540, United States; orcid.org/0000-0003-3459-4241; Email: lschoop@princeton.edu

# **Authors**

Joseph W. Stiles — Department of Chemistry, Princeton University, Princeton, New Jersey 08540, United States; Princeton Materials Institute, Princeton University, Princeton, New Jersey 08540, United States; orcid.org/0000-0003-3128-036X

Brianna Hoff – Department of Chemistry, Princeton University, Princeton, New Jersey 08540, United States

Maria C. Curria — Department of Civil and Environmental Engineering, Princeton University, Princeton, New Jersey 08540, United States; orcid.org/0000-0002-3080-8508

Scott B. Lee — Department of Chemistry, Princeton University, Princeton, New Jersey 08540, United States; ocid.org/0000-0003-0709-935X

Fang Yuan — Department of Chemistry, Princeton University, Princeton, New Jersey 08540, United States; ocid.org/0000-0001-7286-3233

- Guangming Cheng Princeton Materials Institute, Princeton University, Princeton, New Jersey 08540, United States; orcid.org/0000-0001-5852-1341
- Fatmagül Katmer Department of Chemistry, Princeton University, Princeton, New Jersey 08540, United States; orcid.org/0000-0003-1644-4725
- Grigorii Skorupskii Department of Chemistry, Princeton University, Princeton, New Jersey 08540, United States
- Jiaze Xie Department of Chemistry, Princeton University, Princeton, New Jersey 08540, United States
- Josh Leeman Department of Electrical Engineering, Princeton University, Princeton, New Jersey 08540, United States
- Nan Yao Princeton Materials Institute, Princeton University, Princeton, New Jersey 08540, United States; orcid.org/ 0000-0002-4081-1495
- Claire E. White Department of Civil and Environmental Engineering and Andlinger Center for Energy and the Environment, Princeton University, Princeton, New Jersey 08540, United States; © orcid.org/0000-0002-4800-7960
- Craig B. Arnold Department of Mechanical and Aerospace Engineering, Princeton University and Princeton Materials Institute, Princeton University, Princeton, New Jersey 08540, United States; orcid.org/0000-0002-0293-5411

Complete contact information is available at: https://pubs.acs.org/10.1021/acs.chemmater.4c01232

#### **Notes**

The authors declare no competing financial interest.

## ACKNOWLEDGMENTS

The authors thank the Princeton Center for Complex Materials, the Materials Research and Engineering Center, and the National Science Foundation (NSF)-MRSEC program (DMR-2011750) for support. Additionally, the use of the Princeton Imaging and Analysis Center, which is partially supported by the Princeton Center for Complex Materials, the National Science Foundation (NSF)-MRSEC program (DMR-2011750), was crucial to this project. The authors also thank the Princeton Catalysis Initiative and the DOD's Office for Naval Research (ONR), Award No. N00014-21-1-2733, for additional support. This work is based on research conducted at the Center for High-Energy X-ray Sciences (CHEXS), which is supported by the National Science Foundation (BIO, ENG, and MPS Directorates) under award DMR-1829070. B.L.H. and S.B.L are supported by the NSF Graduate Research Fellowship Program under grant number DGE-2039656. Any opinions, findings, conclusions, or recommendations expressed in this material are those of the author(s) and do not necessarily reflect the views of the National Science Foundation.

#### REFERENCES

- (1) Huang, J.; Ouyang, B.; Zhang, Y.; Yin, L.; Kwon, D.-H.; Cai, Z.; Lun, Z.; Zeng, G.; Balasubramanian, M.; Ceder, G. Inhibiting collective cation migration in Li-rich cathode materials as a strategy to mitigate voltage hysteresis. *Nat. Mater.* **2023**, *22*, 353–361.
- (2) Chu, S.; Kim, D.; Choi, G.; Zhang, C.; Li, H.; Pang, W. K.; Fan, Y.; D'Angelo, A. M.; Guo, S.; Zhou, H. Revealing the Origin of Transition-Metal Migration in Layered Sodium-Ion Battery Cathodes: Random Na Extraction and Na-Free Layer Formation. *Angew. Chem. Int. Ed.* **2023**, *62*, No. e202216174.

- (3) McColl, K.; House, R. A.; Rees, G. J.; Squires, A. G.; Coles, S. W.; Bruce, P. G.; Morgan, B. J.; Islam, M. S. Transition metal migration and O<sub>2</sub> formation underpin voltage hysteresis in oxygenredox disordered rocksalt cathodes. *Nat. Commun.* **2022**, *13*, No. 5275.
- (4) Liu, Y.; Rong, X.; Bai, R.; Xiao, R.; Xu, C.; Zhang, C.; Xu, J.; Yin, W.; Zhang, Q.; Liang, X.; et al. Identifying the intrinsic anti-site defect in manganese-rich NASICON-type cathodes. *Nat. Energy* **2023**, *8*, 1088–1096.
- (5) Choe, J.; Yuk, J. M. Capturing and reducing defects. *Nat. Energy* **2023**, *8*, 1063–1064.
- (6) Tapia-Ruiz, N.; Armstrong, A. R.; Alptekin, H.; Amores, M. A.; Au, H.; Barker, J.; Boston, R.; Brant, W. R.; Brittain, J. M.; Chen, Y.; et al. 2021 roadmap for sodium-ion batteries. *J. Phys.: Energy* **2021**, *3*, No. 031503.
- (7) Hestenes, J. C.; Sadowski, J. T.; May, R.; Marbella, L. E. Transition metal dissolution mechanisms and impacts on electronic conductivity in composite LiNi<sub>0.5</sub>Mn<sub>1.5</sub>O<sub>4</sub> cathode films. *ACS Mater. Au* **2023**, *3*, 88–101.
- (8) Geng, F.; Yang, Q.; Li, C.; Hu, B.; Zhao, C.; Shen, M.; Hu, B. Operando EPR and EPR imaging study on a NaCrO<sub>2</sub> cathode: electronic property and structural degradation with Cr dissolution. *J. Phys. Chem. Lett.* **2021**, *12*, 781–786.
- (9) Lyu, Y.; Wu, X.; Wang, K.; Feng, Z.; Cheng, T.; Liu, Y.; Wang, M.; Chen, R.; Xu, L.; Zhou, J.; et al. An overview on the advances of  $LiCoO_2$  cathodes for lithium-ion batteries. *Adv. Energy Mater.* **2021**, 11, No. 2000982.
- (10) Xiao, B.; Wang, Y.; Tan, S.; Song, M.; Li, X.; Zhang, Y.; Lin, F.; Han, K. S.; Omenya, F.; Amine, K.; et al. Vacancy-enabled O3 phase stabilization for manganese-rich layered sodium cathodes. *Angew. Chem. Int. Ed.* **2021**, *60*, 8258–8267.
- (11) Shadike, Z.; Zhou, Y.-N.; Chen, L.-L.; Wu, Q.; Yue, J.-L.; Zhang, N.; Yang, X.-Q.; Gu, L.; Liu, X.-S.; Shi, S.-Q.; Fu, Z. W. Antisite occupation induced single anionic redox chemistry and structural stabilization of layered sodium chromium sulfide. *Nat. Commun.* **2017**, *8*, No. 566.
- (12) Silván, B.; Gonzalo, E.; Djuandhi, L.; Sharma, N.; Fauth, F.; Saurel, D. On the dynamics of transition metal migration and its impact on the performance of layered oxides for sodium-ion batteries: NaFeO<sub>2</sub> as a case study. *J. Mater. Chem. A* **2018**, *6*, 15132–15146.
- (13) Abraham, K. M. How comparable are sodium-ion batteries to lithium-ion counterparts? ACS Energy Lett. 2020, 5, 3544–3547.
- (14) Hwang, J.-Y.; Myung, S.-T.; Sun, Y.-K. Sodium-ion batteries: present and future. *Chem. Soc. Rev.* **2017**, *46*, 3529–3614.
- (15) Wei, Z.; Wang, D.; Yang, X.; Wang, C.; Chen, G.; Du, F. From crystalline to amorphous: an effective avenue to engineer high-performance electrode materials for sodium-ion batteries. *Adv. Mater. Interfaces* **2018**, *5*, No. 1800639.
- (16) Liu, Y.; Xu, Y.; Han, X.; Pellegrinelli, C.; Zhu, Y.; Zhu, H.; Wan, J.; Chung, A. C.; Vaaland, O.; Wang, C.; Hu, L. Porous amorphous FePO<sub>4</sub> nanoparticles connected by single-wall carbon nanotubes for sodium ion battery cathodes. *Nano Lett.* **2012**, *12*, 5664–5668.
- (17) Uchaker, E.; Zheng, Y.; Li, S.; Candelaria, S.; Hu, S.; Cao, G. Better than crystalline: amorphous vanadium oxide for sodium-ion batteries. *J. Mater. Chem. A* **2014**, *2*, 18208–18214.
- (18) Venkatesh, G.; Pralong, V.; Lebedev, O.; Caignaert, V.; Bazin, P.; Raveau, B. Amorphous sodium vanadate  $Na_{1.5+y}VO_3$ , a promising matrix for reversible sodium intercalation. *Electrochem. Commun.* **2014**, 40, 100–102.
- (19) Sun, J.; Zheng, G.; Lee, H.-W.; Liu, N.; Wang, H.; Yao, H.; Yang, W.; Cui, Y. Formation of stable phosphorus—carbon bond for enhanced performance in black phosphorus nanoparticle—graphite composite battery anodes. *Nano Lett.* **2014**, *14*, 4573–4580.
- (20) Song, X.; Cheng, G.; Weber, D.; Pielnhofer, F.; Lei, S.; Klemenz, S.; Yeh, Y.-W.; Filsinger, K. A.; Arnold, C. B.; Yao, N.; Schoop, L. M. Soft chemical synthesis of H<sub>x</sub>CrS<sub>2</sub>: an antiferromagnetic material with alternating amorphous and crystalline layers. *J. Am. Chem. Soc.* **2019**, *141*, 15634–15640.

- (21) Stiles, J. W.; Soltys, A. L.; Song, X.; Lapidus, S. H.; Arnold, C. B.; Schoop, L. M. Unlocking High Capacity and Fast Na+ Diffusion of HxCrS2 by Proton-Exchange Pretreatment. *Adv. Mater.* **2023**, *35*, No. 2209811.
- (22) Bashian, N. H.; Abdel-Latif, S.; Zuba, M.; Griffith, K. J.; Ganose, A. M.; Stiles, J. W.; Zhou, S.; Scanlon, D. O.; Piper, L. F.; Melot, B. C. Transition Metal Migration Can Facilitate Ionic Diffusion in Defect Garnet-Based Intercalation Electrodes. *ACS Energy Lett.* **2020**, *5*, 1448–1455.
- (23) Romero Millán, L. M.; Ghogia, A. C.; White, C. E.; Nzihou, A. Iron nanoparticles to catalyze graphitization of cellulose for energy storage applications. *ACS Appl. Nano Mater.* **2023**, *6*, 3549–3559.
- (24) Wang, Z.; Chan, C. L. C.; Zhao, T. H.; Parker, R. M.; Vignolini, S. Recent Advances in Block Copolymer Self-Assembly for the Fabrication of Photonic Films and Pigments. *Adv. Opt. Mater.* **2021**, *9*, No. 2100519.
- (25) Zeng, X.; Chen, J.; Ma, L.; Chen, C.; Yuan, Y.; Liao, L.; Peng, Z.; Zheng, L.; Huang, Y.; Peng, J.; et al. Cr2S3 nanosheet grafted with porous N-doped carbon architecture as an anode with enhanced Listorage property. *J. Alloys Compd.* **2023**, *966*, No. 171617.
- (26) Cui, F.; Zhao, X.; Xu, J.; Tang, B.; Shang, Q.; Shi, J.; Huan, Y.; Liao, J.; Chen, Q.; Hou, Y.; et al. Controlled growth and thickness-dependent conduction-type transition of 2D ferrimagnetic Cr<sub>2</sub>S<sub>3</sub> semiconductors. *Adv. Mater.* **2020**, 32, No. 1905896.
- (27) Mugiraneza, S.; Hallas, A. M. Tutorial: a beginner's guide to interpreting magnetic susceptibility data with the Curie-Weiss law. *Commun. Phys.* **2022**, *5*, 95.
- (28) Jiménez-Mier, J.; Olalde-Velasco, P.; Yang, W.-L.; Denlinger, J. X-ray absorption and resonant inelastic x-ray scattering (RIXS) show the presence of Cr+ at the surface and in the bulk of CrF2. *AIP Conf. Proc.* **2015**, No. 020002.
- (29) McPherson, G. L.; Devaney, K. EPR spectra of Cr3+ and Cr+centres in the linear-chain lattices, CsMgCl3, CsMgBr3 and CsCdBr3. *J. Phys. C: Solid State Phys.* **1980**, *13*, 1735.
- (30) Zhou, W.; Thompson, J. R.; Leznoff, C. C.; Leznoff, D. B. The Redox-Active Chromium Phthalocyanine System: Isolation of Five Oxidation States from Pc4- CrI to Pc2- CrIII. *Chem.—A Euro. J.* **2017**, 23, 2323—2331.
- (31) Tromp, M.; Moulin, J.; Reid, G.; Evans, J. Cr K-Edge XANES Spectroscopy: Ligand and Oxidation State Dependence—What is Oxidation State? *AIP Conf. Proc.* **2007**, 699–701.
- (32) Xie, J.; Pan, J.-A.; Cheng, B.; Ma, T.; Filatov, A. S.; Patel, S. N.; Park, J.; Talapin, D. V.; Anderson, J. S. Presynthetic Redox Gated Metal-to-Insulator Transition and Photothermoelectric Properties in Nickel Tetrathiafulvalene-Tetrathiolate Coordination Polymers. *J. Am. Chem. Soc.* **2022**, *144*, 19026–19037.
- (33) Westre, T. E.; Kennepohl, P.; DeWitt, J. G.; Hedman, B.; Hodgson, K. O.; Solomon, E. I. A multiplet analysis of Fe K-edge 1s → 3d pre-edge features of iron complexes. *J. Am. Chem. Soc.* **1997**, *119*, 6297–6314.
- (34) Carter, R. L. Molecular Symmetry and Group Theory; John Wiley & Sons, 1997.
- (35) Iglesias-Juez, A.; Chiarello, G. L.; Patience, G. S.; Guerrero-Pérez, M. O. Experimental methods in chemical engineering: X-ray absorption spectroscopy—XAS, XANES, EXAFS. *Can. J. Chem. Eng.* **2022**, *100*, 3–22.
- (36) Bukowski, W. The effect of diglyme on the kinetics of chromium (III) ethanoate-catalyzed reactions of carboxylic acids with epichlorohydrin. *Org. Process Res. Dev.* **2002**, *6*, 10–14.
- (37) Samuel, P. P.; Neufeld, R.; Mondal, K. C.; Roesky, H. W.; Herbst-Irmer, R.; Stalke, D.; Demeshko, S.; Meyer, F.; Rojisha, V. C.; De, S.; et al. Cr (I) Cl as well as Cr+ are stabilised between two cyclic alkyl amino carbenes. *Chem. Sci.* **2015**, *6*, 3148–3153.
- (38) Hibble, S. J.; Walton, R. I.; Pickup, D. M. Local structures of the amorphous chromium sulfide, CrS<sub>3</sub>, and selenide, CrSe<sub>3</sub>, from X-ray absorption studies. *J. Chem. Soc., Dalton Trans.* **1996**, 2245–2251.
- (39) Hibble, S. J.; Walton, R. I.; Hannon, A. C.; Bushnell-Wye, G. The Structure of Amorphous CrS<sub>3</sub> Containing [CrIII2 ((S-I)2)3] x

- Chains: An X-Ray Diffraction Modeling Study. J. Solid State Chem. 1999, 145, 573-579.
- (40) Kang, S. D.; Kuo, J. J.; Kapate, N.; Hong, J.; Park, J.; Chueh, W. C. Galvanostatic intermittent titration technique reinvented: part ii. experiments. *J. Electrochem. Soc.* **2021**, *168*, No. 120504.
- (41) Perl, J.; Shin, J.; Schümann, J.; Faddegon, B.; Paganetti, H. TOPAS: an innovative proton Monte Carlo platform for research and clinical applications. *Med. Phys.* **2012**, *39*, 6818–6837.
- (42) Faddegon, B.; Ramos-Méndez, J.; Schuemann, J.; McNamara, A.; Shin, J.; Perl, J.; Paganetti, H. The TOPAS tool for particle simulation, a Monte Carlo simulation tool for physics, biology and clinical research. *Physica Medica* **2020**, 72, 114–121.
- (43) Bruker. Apex 2 (v2014.11-0); Bruker AXS Inc.: Madison, Wisconsin, USA, 2012.
- (44) Juhás, P.; Davis, T.; Farrow, C. L.; Billinge, S. J. PDFgetX3: a rapid and highly automatable program for processing powder diffraction data into total scattering pair distribution functions. *J. Appl. Crystallogr.* **2013**, *46*, 560–566.
- (45) Farrow, C. L.; Juhas, P.; Liu, J.; Bryndin, D.; Božin, E.; Bloch, J.; Proffen, T.; Billinge, S. PDFfit2 and PDFgui: computer programs for studying nanostructure in crystals. *J. Phys.: Condens. Matter* **2007**, *19*, No. 335219.
- (46) Kresse, G.; Furthmuller, J. Efficiency of ab-initio total energy calculations for met- als and semiconductors using a plane-wave basis set. *Comput. Mater. Sci.* **1996**, *6*, 15–50.
- (47) Kresse, G.; Furthmuller, J. Efficient iterative schemes for ab initio total-energy calculations using a plane-wave basis set. *Phys. Rev. B* **1996**, *54*, No. 11169.
- (48) Perdew, J. P.; Burke, K.; Ernzerhof, M. Generalized gradient approximation made simple. *Phys. Rev. Lett.* **1996**, *77*, 3865–3869.
- (49) Blöchl, P. E. Projector augmented-wave method. *Phys. Rev. B* **1994**, *50*, No. 17953.
- (50) Kresse, G.; Joubert, D. From ultrasoft pseudopotentials to the projector augmented- wave method. *Phys. Rev. B* **1999**, *59*, 1758.
- (51) Ushakov, A. V.; Kukusta, D.; Yaresko, A.; Khomskii, D. Magnetism of layered chromium sulfides MCrS<sub>2</sub> (M = Li, Na, K, Ag, and Au): a first-principles study. *Phys. Rev. B* **2013**, 87, No. 014418.
- (52) Monkhorst, H. J.; Pack, J. D. Special points for Brillouin-zone integrations. *Phys. Rev. B* **1976**, *13*, 5188.
- (53) Rüdorff, W.; Stegemann, K. Kristallstruktur und magnetisches Verhalten der Alkalithiochromite. Z. Anorg. Allg. Chem. 1943, 251, 376–395.
- (54) Newville, M. Larch: an analysis package for XAFS and related spectroscopies. J. Phys.: Conf. Ser. 2013, 430, No. 012007.
- (55) Westman, K.; Dugas, R.; Jankowski, P.; Wieczorek, W.; Gachot, G.; Morcrette, M.; Irisarri, E.; Ponrouch, A.; Palacín, M. R.; Tarascon, J.-M.; Johansson, P. Diglyme based electrolytes for sodium-ion batteries. ACS Applied Energy Materials 2018, 1, 2671–2680.